RSC Advances

PAPER

View Article Online
View Journal | View Issue

Cite this: *RSC Adv.*, 2025, **15**, 3040

Facile synthesis of an α-Fe_2O_3–TiO_2-MXene heterojunction for enhanced acetone gas sensors

Zhenyuan Yang[ab] and Ying Chen *[ab]

Received 28th November 2024
Accepted 14th January 2025

DOI: 10.1039/d4ra08407a

rsc.li/rsc-advances

Acetone is harmful to the environment and human health. Therefore, research on acetone sensors for its high-efficiency detection is necessary. Herein, an α-Fe_2O_3–TiO_2-MXene heterojunction was synthesized using a simple precipitation method, and its sensitivity towards acetone was systematically investigated. The response value of the sensor based on the α-Fe_2O_3–TiO_2-MXene heterojunction to 50 ppm acetone was 24 at 150 °C, which was more than one-quarter of that of pure α-Fe_2O_3 (5.3). The best response and recovery time were 10 s and 6 s, respectively. The sensors also showed good stability and selectivity. The excellent gas sensitivity was mainly attributed to the formation of heterojunctions, which improved the carrier-transport efficiency and the specific surface area for gas molecular adsorption.

Introduction

Acetone is a common volatile organic compound (VOC), which can greatly harm the human throat, liver, kidney, and nerves if inhaled in a certain amount.[1] It is also an important biomarker in human breath, which can be used for the preliminary review and diagnosis of diabetes.[2] Therefore, the development of a high-performance acetone sensor could not only allow the monitoring of air quality in real-time but would also be beneficial for human health.[3]

In recent years, ZnO,[4] WO_3,[5] TiO_2,[6] SnO_2,[7] NiO,[8] Co_3O_4,[9] α-Fe_2O_3,[10] and other metal oxide semiconductors have been developed in the field of gas sensing. Among them, α-Fe_2O_3 is an n-type semiconductor material with a band-gap of 2.2 eV, which offers the advantages of low cost, good stability, and non-toxicity, and it is harmless.[11–13] Although α-Fe_2O_3 exhibits good gas-sensing properties, it usually requires a higher operating temperature and gives a slower response, which limits its application in portable and low-power devices.[14] Various materials have been employed to blend with α-Fe_2O_3 to improve its performance.[15–19] Zhang *et al.* formed a heterojunction of α-Fe_2O_3 and $Ti_3C_2T_x$ MXene, which accelerated the carrier-transport efficiency, enlarged the specific surface area with more active sites, and thus improved its H_2S gas-sensing property.[20] Song *et al.* successfully synthesized a Fe_2O_3/$Ti_3C_2T_x$ MXene heterojunction *via* an *in situ* growth method. The sensor's response was 1.31 to 70 ppb *n*-butanol.[21] Liu *et al.* used gold nanoparticles to modify the surface of α-Fe_2O_3/$Ti_3C_2T_x$ MXene composites. The sensor's response value to 1 ppm NH_3 reached 16.9% at room temperature.[22]

Herein, an α-Fe_2O_3–TiO_2-MXene heterojunction was successfully synthesized *via* a simple precipitation method. The thin sheet structure of α-Fe_2O_3 was evenly distributed on the accordion-like structure of $Ti_3C_2T_x$ MXene, which provided more active sites for gas molecular adsorption. The formation of a heterojunction also improved the carrier-transport efficiency. The response value of the sensor based on the α-Fe_2O_3–TiO_2-MXene heterojunction to 50 ppm acetone was 24 at 150 °C with a response/recovery time of 10 s/6 s.

Materials and methods

Synthesis of $Ti_3C_2T_x$ MXene and α-Fe_2O_3–TiO_2-$Ti_3C_2T_x$ MXene

Chemical reagents. Hydrofluoric acid (HF, 40%), ferrous sulfate ($FeSO_4 \cdot 7H_2O$, AR), and sodium acetate (CH_3COONa, AR) were purchased from Sinopharm Group Chemical Co., Ltd. Ti_3AlC_2 (99%) was purchased from Jilin 11 Technology Co., Ltd. Deionized (DI) water was made in the laboratory.

Synthesis of $Ti_3C_2T_x$ MXene. $Ti_3C_2T_x$ MXene was synthesized by etching Ti_3AlC_2 with HF. Next, 1 g of Ti_3AlC_2 was slowly added to 20 mL of 40% HF with stirring. After stirring at 60 °C for 24 h, the obtained black solution was centrifuged and washed with deionized water. The centrifugal speed was 4000 rpm, and the time was 10 min. The mixtures were centrifuged and washed several times until the supernatant pH was 7. The precipitation was vacuum dried at 60 °C for 48 h and then triturated to obtain $Ti_3C_2T_x$ MXene as a multilayer black powder.

Synthesis of α-Fe_2O_3. α-Fe_2O_3 was synthesized by a precipitation method. First, 0.556 g of $FeSO_4 \cdot 7H_2O$ and 0.3 g of CH_3COONa were added to 60 mL deionized water and then stirred for 12 h at room temperature. Then the mixture was centrifuged

[a]School of Science, Hubei University of Technology, Wuhan 430068, China. E-mail: chenying@hbut.edu.cn
[b]Hubei Engineering Technology Research Center of Energy Photoelectric Device and System, Hubei University of Technology, Wuhan 430068, China

and washed several times with deionized water and ethanol. After being dried h at 80 °C for 10 h, the precipitations were calcined at 600 °C for 2 h to obtain the α-Fe_2O_3 powders. The synthesis process was repeated three times under the same experimental conditions as above to conduct error analysis in the subsequent test of the gas sensor performance. Synthesis of α-Fe_2O_3–TiO_2-MXene composite materials followed the same method.

Synthesis of α-Fe_2O_3–TiO_2-MXene. A series of α-Fe_2O_3–TiO_2-MXenes in different proportions were synthesized by a precipitation method. First, 0.01, 0.03, 0.05, and 0.1 g $Ti_3C_2T_x$ MXenes were ultrasonically dispersed in 50 mL of deionized water, respectively. Then, to each $Ti_3C_2T_x$ MXene water solution was added 0.556 g of $FeSO_4 \cdot 7H_2O$ and 0.3 g of CH_3COONa to obtain a mixture. These mixtures were continuously stirred for 12 h at room temperature. These mixtures were then centrifuged and washed several times with deionized water and ethanol. After being dried at 80 °C for 10 h, the precipitations were calcined at 600 °C for 2 h to obtain the different samples of α-Fe_2O_3–TiO_2-MXene, which were named M-F-0.01, M-F-0.03, M-F-0.05, and M-F-0.1, respectively.

Characterization

The material crystal structures were characterized by X-ray diffraction (XRD, Rigaku D/Max2550, Tokyo, Japan) with Cu Kα radiation (λ = 1.5418 Å). The scanning range was 5°–80°. Their morphologies were observed by field-emission scanning electron microscopy (FESEM, Hitachi SU8010, Japan) and transmission electron microscopy (TEM, FEI Tecnai F20, USA). The element contents of all the samples were analyzed using an energy-dispersive X-ray spectroscopy (EDS) unit attached to the FESEM device. The elemental chemical status and compositions were identified by X-ray photoelectron spectroscopy (XPS) with Al Kα (1486.6 eV) excitation.

Sensor preparation and testing

The preparation of the sensors was as follows: first, the appropriate sample powders and deionized water were mixed to form a paste. Then, the paste was brushed evenly on the Al_2O_3 ceramic surface. After drying at 160 °C for 10 h, the Al_2O_3 ceramic and the sensor base were welded together. Finally, the sensor was aged at 180 °C for 48 h before the test.

The gas-sensitive performance was measured by a WS-30B gas-sensitive test system (Henan Weisheng Electronic Technology Co., Ltd, China), as shown in Fig. 1(b). The test system was composed of sensor resistance R_S, load resistance R_L, and current source V_C, and the working temperature of the sensor was adjusted by changing the value of V_H. By measuring the voltage V_{output} at both ends of the load resistance, then the sensor resistance value can be obtained from formula (1).

$$R_S = \frac{(V_C - V_{output})R_L}{V_{output}} \quad (1)$$

In the test process, the measured liquid was dropped on to the evaporator with a syringe and heated to vaporize it into a gas.

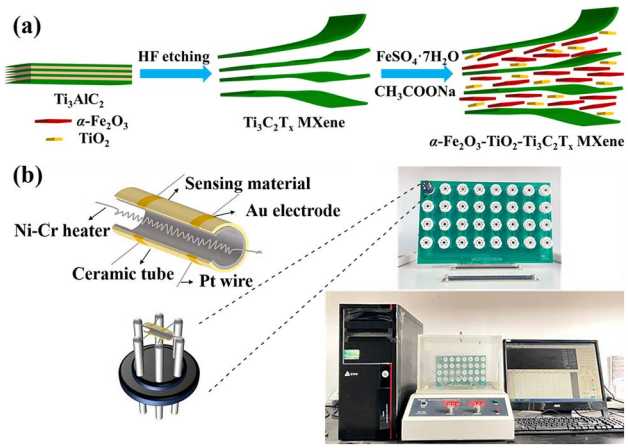

Fig. 1 Schematic of the (a) α-Fe_2O_3–TiO_2-MXene preparation process and (b) gas sensor test.

The relationship between the injection volume and the concentration can be determined according to formula (2).

$$V_X = \frac{V \times C \times M}{22.4 \times d \times p} \times 10^{-9} \times \frac{273 + T_R}{273 + T_B} \quad (2)$$

where V_X is the volume of the injected liquid (mL), V is the volume of the test chamber (18 L), C is the required concentration of the gas to be measured (ppm), M is the molecular weight of the liquid (g), d is the specific gravity of the liquid (g cm^{-3}), p is the liquid purity, T_R is room temperature (°C), and T_B is the temperature in the test chamber (°C).

The response value S can be calculated using the formula $S = R_a/R_g$, where R_a is the resistance value of the sensor in air and R_g is the resistance value of the sensor in the test gas.

Results and discussion

Structure and morphology

As shown in Fig. 2(a), the diffraction peak of Ti_3AlC_2 matched the standard card (JCPDS: 52-0875) without impurities. Comparing the XRD pattern of $Ti_3C_2T_x$ MXene with Ti_3AlC_2, the impurity peaks were weakened, while the (002) peak for $Ti_3C_2T_x$ MXene was shifted from 9.45° to 8.75°. The HF etching removed the Al layer and enlarged the layer spacing. These findings prove that $Ti_3C_2T_x$ MXene was successfully synthesized.[23] The α-Fe_2O_3 in Fig. 2(b) corresponded to the standard card (JCPDS: 33-0664). In the etching process of Ti_3AlC_2, HF removes its Al layer, then

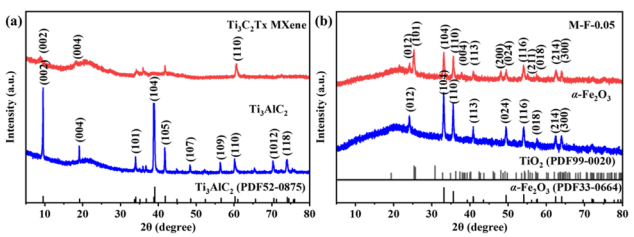

Fig. 2 XRD patterns of (a) Ti_3AlC_2 and $Ti_3C_2T_x$ MXene, (b) α-Fe_2O_3 and M-F-0.05.

the Ti atoms in $Ti_3C_2T_x$ are converted to Ti^{3+} under acidic conditions. These ions are then oxidized to TiO_2 at $Ti_3C_2T_x$ defects. The peaks (101), (004), (200), and (211) of M-F-0.05 were due to the oxidation of $Ti_3C_2T_x$ MXene to TiO_2 at 600 °C. The content of $Ti_3C_2T_x$ MXene was low. So, the other peaks of M-F-0.05 were consistent with α-Fe_2O_3.[19]

As shown in Fig. 3(a), the Ti_3AlC_2 surface layers fitted closely without stratification. After being etched by HF, Ti_3AlC_2 lost the middle Al layer and became an accordion-like structure for $Ti_3C_2T_x$ MXene (Fig. 3(b)). α-Fe_2O_3 displayed a relatively thin sheet structure (Fig. 3(c)). When α-Fe_2O_3 and $Ti_3C_2T_x$ MXene formed a complex, as shown in the M-F-0.05 SEM image of Fig. 3(d), α-Fe_2O_3 was evenly distribute on the surface of $Ti_3C_2T_x$ MXene. The EDS element mapping images of M-F-0.05 are shown in Fig. 3(f). The Ti, O, Fe, and C elements were evenly distributed in the composite material, which indicated that the α-Fe_2O_3–TiO_2-MXene composite material had been successfully synthesized.

TEM and HRTEM images of M-F-0.05 were obtained. In Fig. 4(e), the observed lattice spacing of 0.246 nm corresponded to the (021) crystal surface of TiO_2, as shown by red dotted rectangles (Fig. 4(b) and (c)). In Fig. 4(f), the lattice spacing of 0.354 nm corresponded to the (012) crystal surface of α-Fe_2O_3, as shown by the yellow dotted rectangles (Fig. 4(b) and (c)). In Fig. 4(g), the lattice spacing of 0.249 nm corresponded to the (102) crystal surface of $Ti_3C_2T_x$ MXene, as shown by the white dotted rectangles (Fig. 4(b) and (d)).[19,22] These results were consistent with the XRD results.

The XPS high-resolution spectra of α-Fe_2O_3 are shown in Fig. 5(a) and (b). Fig. 5(a) is the Fe 2p high-resolution spectra of α-Fe_2O_3. The peaks at binding energies of 723.9 and 710.2 eV

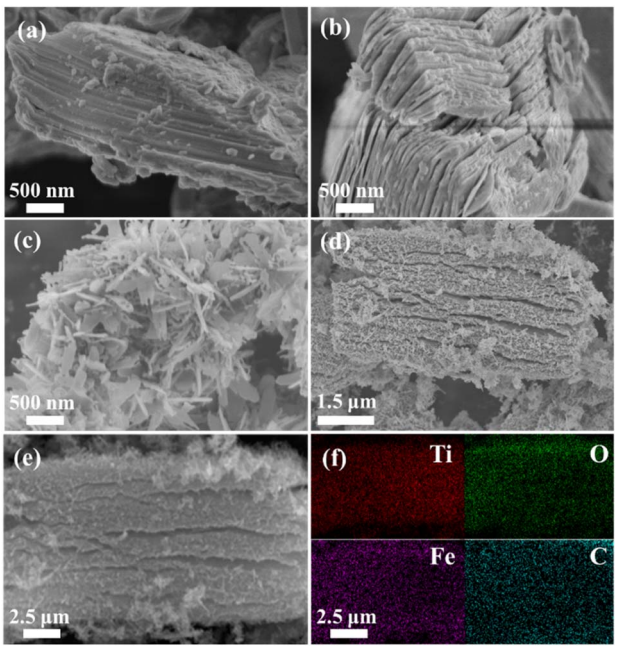

Fig. 3 SEM characterization of (a) Ti_3AlC_2, (b) $Ti_3C_2T_x$ MXene, (c) α-Fe_2O_3, (d) and (e) M-F-0.05. (f) EDS mapping for Ti, O, Fe, and C of M-F-0.05.

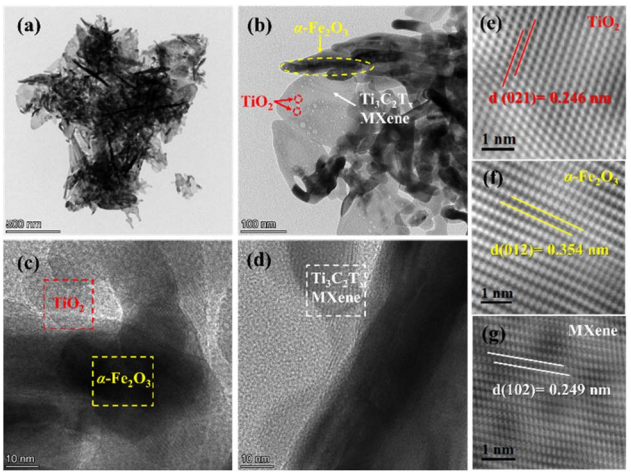

Fig. 4 (a) and (b) TEM characterization of M-F-0.05, (c)–(g) HRTEM characterization of M-F-0.05.

were attribute to Fe $2p_{1/2}$ and Fe $2p_{3/2}$, respectively. The satellite peaks centered around 725.3 and 718.2 eV were from Fe^{3+}, indicating the successful synthesis of α-Fe_2O_3.[24] Fig. 5(b) presents the O 1s spectrum, which was mainly divided into three peaks, with peaks at binding energies of 531.7, 530.6, and 529.1 eV, corresponding to H–O–H, Fe–OH, and Fe–O bonds, respectively.[25]

The XPS high-resolution spectra of the M-F-0.05 heterojunction are shown in Fig. 5(c)–(f). Fig. 5(c) shows the high-resolution spectrum of Fe 2p of M-F-0.05. The peaks at

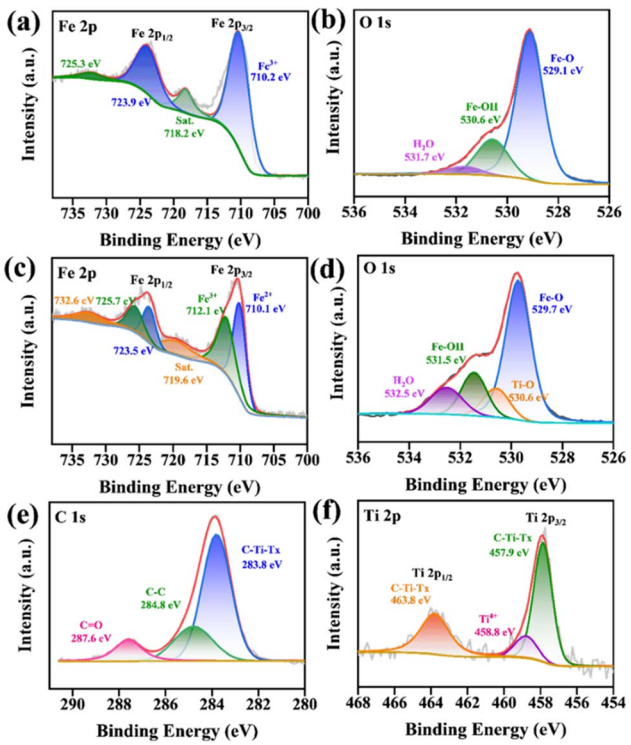

Fig. 5 XPS spectra of α-Fe_2O_3 (a) Fe 2p and (b) O 1s. XPS spectra of M-F-0.05 heterojunction: (c) Fe 2p, (d) O 1s, (e) C 1s, and (f) Ti 2p.

binding energies of 723.9 and 710.4 eV corresponded to Fe $2p_{1/2}$ and Fe $2p_{3/2}$, respectively, while those at 710.1 and 723.5 eV were attributed to Fe^{2+}, at 712.1 and 725.7 eV to Fe^{3+}, and 719.6 and 732.6 eV to the satellite peaks of Fe^{3+}.[26] Fig. 5(d) is the high-resolution O 1s spectrum of M-F-0.05 heterojunction. The peaks at binding energies of 532.5, 531.5, 530.6, and 529.7 eV corresponded to H–O–H, Fe–OH, Ti–O, and Fe–O bonds, respectively.[27,28] Fig. 5(e) shows the C 1s high-resolution spectrum of M-F-0.05. The peaks at binding energies of 287.6, 284.8, and 283.8 eV were attributed to C=O, C–C, and C–Ti–T_x, respectively.[29] Fig. 5(f) shows the Ti 2p high-resolution spectrum of M-F-0.05, which could be divided into Ti $2p_{3/2}$ (457.9 eV) and Ti $2p_{1/2}$ (463.8 eV). The peaks at binding energies of 463.8, 458.8, and 457.9 eV were attributed to C–Ti–T_x, Ti^{4+}, and C–Ti–T_x bonds, respectively.[30] The presence of Ti^{4+} indicated that TiO_2 was generated in the hydrothermal process, which was consistent with the results of the XRD analysis above.

Gas-sensitive performance

The operating temperature has a huge impact on the sensor. The lower the temperature, the fewer electrons/holes and the slower the migration rate in the gas-sensitive materials, and the response value is then low or there is even no response. Higher temperature excites more electrons and leads to a faster migration rate of electrons and holes, and so the activity of gas-sensitive materials is increased, and the response value increases accordingly. Too high an operating temperature will accelerate desorption of the gas, which is equivalent to reducing the gas adsorbed on the surface of the material, and the response value will then be reduced. Therefore, we first explored the relationship between the operating temperatures and the gas-sensing performance.[31,32] The gas-response values of α-Fe_2O_3, M-F-0.01, M-F-0.03, M-F-0.05, and M-F-0.1 to 50 ppm acetone at different temperatures (50 °C, 80 °C, 100 °C, 150 °C, 200 °C, and 250 °C) are shown in Fig. 6(a). The best working temperature of the sensor was 150 °C. Moreover, with the increase in $Ti_3C_2T_x$ MXene content, α-Fe_2O_3–TiO_2-MXene had more heterojunctions. The sensors based on M-F-0.05 showed the maximum response values at each temperature. However, the sensor based on M-F-0.1 had the smaller response values. This was possibly because excessive $Ti_3C_2T_x$ MXene addition will lead to a stacking of the sheets, which reduces the adsorption sites and affects the gas-sensitive response of the composite.[33] Each group of experiments above tested three groups of gas sensors under the same experimental conditions, and the mean value and standard deviation were taken, and then the error bar was obtained, which represents the label difference, while the length of the error bar also represents the degree of data dispersion. The same was true for the subsequent gas-sensitivity tests. Fig. 6(b) presents the dynamic response curve of the sample to different concentrations of acetone gas at 150 °C. The response value increased with the increasing acetone concentration. The response of M-F-0.05 to 50 ppm acetone was 24, while that of α-Fe_2O_3 was 5.3.

The response/recovery curves of different samples to different concentrations of acetone gas at 150 °C are shown in Fig. 7(a)–(e). Under the same test conditions, sensor M-F-0.05 had the shortest response/recovery time and the largest response value (10 s/6 s). Repeatability testing of α-Fe_2O_3 and M-F-0.05 in 50 ppm acetone gas at 150 °C was carried out (Fig. 7(f)). The results showed they all had good repeatability.

Selectivity is also one of the main properties of gas sensors. The sensors were tested with 50 ppm of different gases (acetone, ethanol, ammonia, *n*-butanol, ethylene glycol, and isopropyl alcohol) at 150 °C, and the results are shown in Fig. 8(a). M-F-0.05 had the better response to acetone gas compared to the other gases. From the stability tests of α-Fe_2O_3 and M-F-0.05 in 50 ppm acetone gas at 150 °C for 30 days, as shown in Fig. 8(b), M-F-0.05 also demonstrated good stability. Table 1 shows

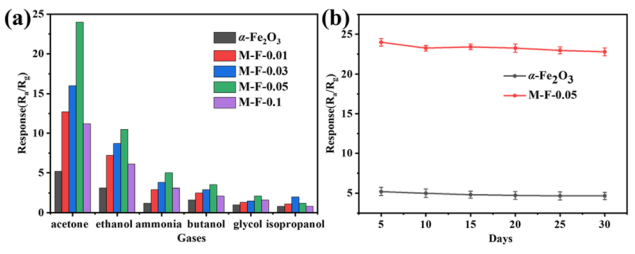

Fig. 6 (a) Response values of α-Fe_2O_3, M-F-0.01, M-F-0.03, M-F-0.05, and M-F-0.1 to 50 ppm acetone at different temperatures. The error bar is from the mean values and standard deviations of three tested groups of gas sensors under the same experimental conditions. (b) Dynamic response values to different concentrations of acetone at 150 °C.

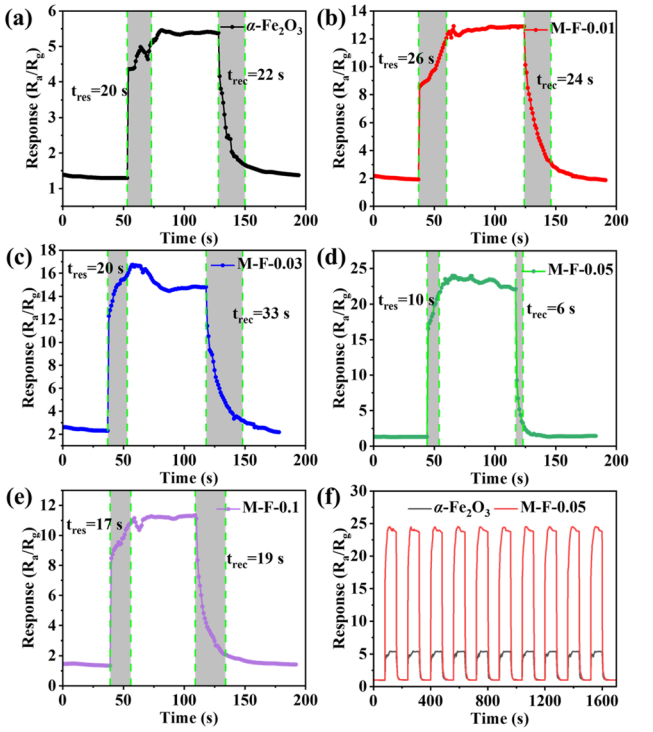

Fig. 7 (a)–(e) α-Fe_2O_3, M-F-0.01, M-F-0.03, M-F-0.05, and M-F-0.1 response/recovery curves to 50 ppm acetone at 150 °C. (f) Repeatability testing of α-Fe_2O_3 and M-F-0.05 in 50 ppm acetone gas at 150 °C.

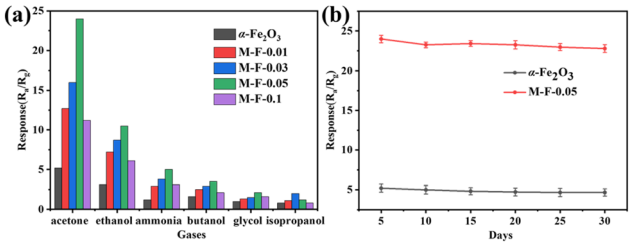

Fig. 8 (a) M-F-0.05 selectivity to 50 ppm of different gases at 150 °C. (b) 30 days stability test of α-Fe_2O_3 and M-F-0.05 in 50 ppm acetone gas at 150 °C. The error bar is from the mean values and standard deviations of three tested groups of gas sensors under the same experimental conditions.

a comparison of the acetone responses between the M-F-0.05 sensor and some relevant reports. The sensor based on M-F-0.05 exhibited a relatively higher acetone response with a lower working temperature, confirming our sensor is a promising candidate for acetone detection with low power consumption.

Gas-sensing mechanism

The gas-sensitive response of the sensing material is affected by the chemical adsorption of oxygen on the semiconductor surface and the chemical reaction of the gas molecules to be measured.[42] The α-Fe_2O_3–TiO_2-MXene gas sensor showed n-type semiconductor characteristics when testing acetone. Here, the oxygen in the air will be adsorbed on its surface, trapping the electrons in its conduction band to generate chemisorbed oxygen (O_2^-), resulting in a widening of the electron depletion layer and increase in the resistance value of the material.[43,44] $Ti_3C_2T_x$ MXene with metallic properties has a work function of 4.37 eV. TiO_2 has a work function of 4.6 eV. After contacting, the electrons in the $Ti_3C_2T_x$ MXene conduction band will be transferred to the TiO_2 conduction band until their Fermi levels reach equilibrium. A Schottky barrier will form at the interface between $Ti_3C_2T_x$ MXene and TiO_2. The work function of α-Fe_2O_3 is 5.9 eV, therefore when it contacts with $Ti_3C_2T_x$ MXene-TiO_2 heterojunction, electrons will be transferred from the $Ti_3C_2T_x$ MXene-TiO_2 heterojunction to α-Fe_2O_3, and then another heterojunction will form between the $Ti_3C_2T_x$ MXene-TiO_2 heterojunction and α-Fe_2O_3. In acetone, acetone molecules are oxidized by oxygen ions (O^-) and release electrons into the conduction band of α-Fe_2O_3–TiO_2-MXene, causing the electron depletion layer to narrow, thus further reducing the resistance value of the material, which plays a crucial role in improving the gas-sensitive performance. The whole reaction process is shown

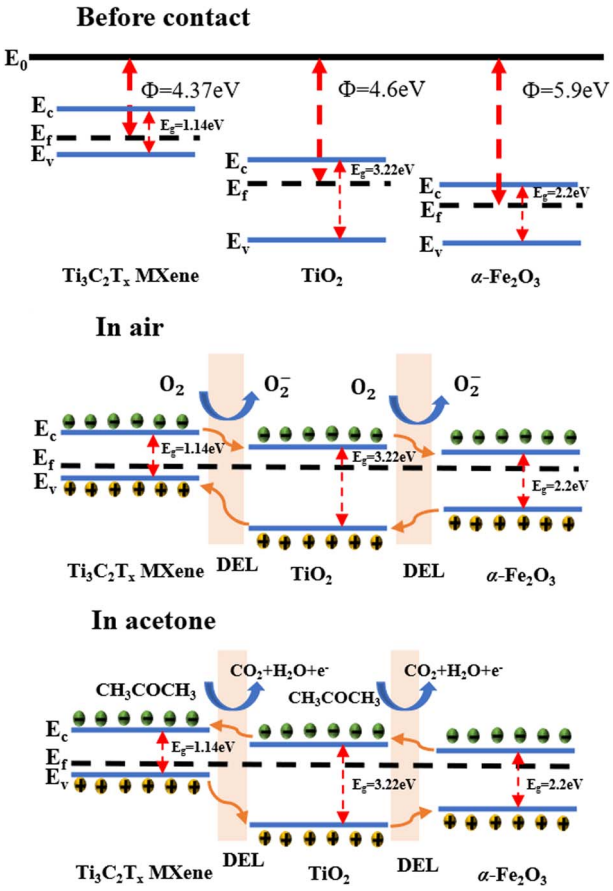

Fig. 9 Schematic of the gas-sensing mechanism of the α-Fe_2O_3–TiO_2-MXene heterojunction-based sensor.

Table 1 Comparison table of different acetone sensors[a]

Sensing materials	Preparation method	Temperature (°C)	Concentration (ppm)	S (R_a/R_g)	Res./Rec. time (s)	Ref.
α-Fe_2O_3	Hydrothermal	400	100	13.1	3/108	12
α-Fe_2O_3	Azeotropic distillation	340	100	9.1	—	34
α-Fe_2O_3/$CuFe_2O_4$	Template	275	100	14	—	35
α-Fe_2O_3/SnO_2	Hydrothermal	280	200	16.8	5/23	36
$ZnFe_2O_4$/Ag	Hydrothermal	175	100	33.4	17/148	37
α-Fe_2O_3/SiO_2	Sol–gel	290	500	50.2	14/7	38
Ce-α-Fe_2O_3	Oil bath	220	100	26.3	7/80	14
$ErFeO_3$/α-Fe_2O_3	Impregnation	250	100	55	9/123	39
Pt-Fe_2O_3	Hydrothermal	139	100	25.7	3/22	40
α-Fe_2O_3/TiO_2@$Ti_3C_2T_x$	Hydrothermal	220	100	34.66	10/7	41
α-Fe_2O_3–TiO_2-MXene	Precipitation	150	50	24	10/6	This work

[a] Res./Rec. Time-response/recovery time.

in eqn (3)–(6).[21,45] The reaction mechanism diagram is shown in Fig. 9.

$$O_2\ (gas) \rightarrow O_2\ (ads) \quad (3)$$

$$O_2\ (ads) + e^- \rightarrow O_2^-\ (ads) \quad (4)$$

$$O_2^-\ (ads) + e^- \rightarrow 2O^-\ (ads) \quad (5)$$

$$CH_3COCH_3\ (gas) + 8O^-\ (ads) \rightarrow 3CO_2\ (ads) + 3H_2O + 8e^- \quad (6)$$

Conclusions

α-Fe_2O_3–TiO_2-MXene heterojunctions were successfully prepared by a simple precipitation method. The gas sensor based on them showed good responses value for 24 to 50 ppm acetone at 150 °C, which was more than a-quarter that of pure α-Fe_2O_3 (5.3). It also had a shorter response/recovery time (10 s/6 s) and a better stability. The enhanced gas sensitivity of the α-Fe_2O_3–TiO_2-MXene gas sensor may be mainly due to two reasons. (1) The α-Fe_2O_3–TiO_2-MXene heterojunction could improve the electron-transfer efficiency. (2) The α-Fe_2O_3–TiO_2-MXene heterojunction has a larger specific surface area with more active sites for gas-sensitive reactions. This article provides an idea for developing excellent acetone sensor-sensitive materials. However, the optimal working temperature needs to be further reduced.

Data availability

Data for this article are available from the Open Science Framework at **https://osf.io/jt7yg**.

Author contributions

Conceptualization, Y. Chen and Z. Y. Yang; validation, Y. Chen and Z. Y. Yang; writing—original draft, Y. Chen and Z. Y. Yang; writing—review & editing, Y. Chen and Z. Y. Yang; visualization, Y. Chen; supervision, Y. Chen. All authors have read and agreed to the published version of the manuscript.

Conflicts of interest

There are no conflicts to declare.

Acknowledgements

This research was funded by the China-Africa Partner Research Institute Exchange Project "China-South Africa Advanced Photovoltaic Hydrogen Energy System Research Center", and the National "111 Research Center" for Microelectronics and Integrated Circuits.

References

1 Y.-N. Wang, L. Qin, Z. Yuan, J. Li and F. Meng, *Sens. Actuators, B*, 2024, **418**, 136283.
2 S. Thangavel, D. Pattappan, P. Subramaniam, S. Srinivasan, S. Madanagurusamy, K. Krishnasamy, Y.-T. Lai and K. Udayar, *Ceram. Int.*, 2024, **50**, 36512–36520.
3 W. Zhang, Y. Xian, B. Cheng, R. Han, Y. Zhang and J. Xiang, *Ceram. Int.*, 2024, **50**, 34027–34036.
4 L. Zhang, F. Li, Y. Yang, D. Li, H. Yu, X. Dong and T. Wang, *Chem. Eng. J.*, 2024, **499**, 156604.
5 R. Xavier, L. Thirumalaisamy, S. Madhanagurusamy and K. Sivaperuman, *Ceram. Int.*, 2024, **50**, 969–976.
6 P. Song and T. Wang, *ACS Sens.*, 2022, **7**, 3634–3643.
7 L. Zhang, J. Tian, Y. Wang, T. Wang, M. Wei, F. Li, D. Li, Y. Yang, H. Yu and X. Dong, *Sens. Actuators, B*, 2024, **410**, 135728.
8 C. Li, P. G. Choi, K. Kim and Y. Masuda, *Sens. Actuators, B*, 2022, **367**, 132143.
9 L. Fu, D. Li and W. Tang, *J. Alloys Compd.*, 2023, **960**, 170648.
10 T. K. Dang, N. D. Cuong, H. V. M. Hai, T. Q. Phuong, L. L. Son, D. T. T. Nhan, V. V. Tan, M. D. Hien, K.-J. Jeon, N. Q. Hung, L. A. Tuyen and N. V. Hieu, *Sens. Actuators, B*, 2023, **383**, 133573.
11 H. Wang, Y. Luo, K. Li, B. Liu, L. Gao and G. Duan, *Chem. Eng. J.*, 2022, **427**, 131631.
12 A. Umar, A. A. Ibrahim, R. Kumar, H. Albargi, M. A. Alsaiari and F. Ahmed, *Sens. Actuators, B*, 2021, **326**, 128851.
13 S. Kumar, M. Hojamberdiev, A. Chakraborty, R. Mitra, R. Chaurasiya, M. Kwoka, C. S. Tiwary, K. Biswas and M. Kumar, *ACS Appl. Nano Mater.*, 2024, **16**, 16687–16698.
14 X. Wang, T. K. Wang, G. K. Si, Y. Li, S. W. Zhang, X. L. Deng and X. J. Xu, *Sens. Actuators, B*, 2020, **302**, 127165.
15 N. Dhariwal, M. Chahar, V. Kumar and O. P. Thakur, *Sens. Actuators, B*, 2023, **390**, 134037.
16 M. Das, A. K. Shringi and M. Kumar, *IEEE Sens. J.*, 2022, **22**, 19183–19190.
17 J. Bian, Y. Zhang, M. Tang, Z. Wang, Q. Chen and D. Zhang, *IEEE Sens. J.*, 2024, **24**, 7456–7462.
18 J. Tang, H. Wang, W. Dong, H. Yang, X. Wang, X. Guo and D. Zeng, *Ceram. Int.*, 2024, **50**, 14151–14160.
19 S. Li, L. Yu, Y. Zhang, C. Zhang, L. Cao, N. Nan, X. Fan and H. Wang, *Sens. Actuators, B*, 2024, **413**, 135890.
20 D. Zhang, J. Jiang, T. Wang, F. Li, H. Yu, X. Dong and Y. Yang, *Sens. Actuators, B*, 2024, **421**, 136543.
21 X. Song, T. Liu, K. Gu, Z. Luo and M. Zhang, *J. Alloys Compd.*, 2024, **976**, 173153.
22 M. Liu, R.-Y. Sun, Y.-L. Ding, Q. Wang and P. Song, *ACS Appl. Nano Mater.*, 2023, **6**, 11856–11867.
23 X. Xu, W. Ma, H. Jiang, X. Wang, W. Liu, M. Wang, G. Sun, N. Ma, S. Ma, J. Wang and G. Chang, *Sens. Actuators, B*, 2025, **422**, 136595.
24 M. Liu, J. Ji, P. Song, J. Wang and Q. Wang, *J. Alloys Compd.*, 2022, **898**, 162812.
25 N. D. Cuong, V. H. Sinh, D. T. Quang, L. T. Hoa, V. V. Tan, H. D. Mai, K.-J. Jeon, P. H. Phuoc and N. V. Hieu, *Curr. Appl. Phys.*, 2024, **59**, 153–164.
26 P. S. Bagus, C. J. Nelin, C. R. Brundle, B. V. Crist, N. Lahiri and K. M. Rosso, *Phys. Chem. Chem. Phys.*, 2022, **24**, 4562–4575.

27 A. Vijaykumar, A. Mondal, S. Deb, B. Ajitha and Y. A. K. Reddy, *Appl. Surf. Sci.*, 2024, **670**, 160664.
28 Y. Qin, Y. Zhang, P. Qiu and S. Lei, *Sens. Actuators, B*, 2025, **422**, 136521.
29 W. Waheed, S. Anwer, M. U. Khan, M. Sajjad and A. Alazzam, *Chem. Eng. J.*, 2024, **480**, 147981.
30 Q. T. H. Ta, A. Sreedhar, N. N. Tri and J.-S. Noh, *Ceram. Int.*, 2024, **50**, 27227–27236.
31 L. Zhang, T. Wang, Y. Yang, M. Wei, F. Li, H. Yu and X. Dong, *J. Alloys Compd.*, 2024, **977**, 173430.
32 P. Li, Y. Yang, F. Li, W. Pei, D. Li, H. Yu, X. Dong and T. Wang, *Sens. Actuators, B*, 2025, **426**, 137111.
33 S. B. Sun, M. W. Wang, X. T. Chang, Y. C. Jiang, D. Z. Zhang, D. S. Wang, Y. L. Zhang and Y. H. Lei, *Sens. Actuators, B*, 2020, **304**, 127274.
34 S. Liang, J. P. Li, F. Wang, J. L. Qin, X. Y. Lai and X. M. Jiang, *Sens. Actuators, B*, 2017, **238**, 923–927.
35 X. Li, D. Lu, C. Shao, G. Lu, X. Li and Y. Liu, *Sens. Actuators, B*, 2018, **258**, 436–446.
36 M. Liu, P. Song, Z. Yang and Q. Wang, *Ceram. Int.*, 2021, **47**, 12181–12188.
37 C. Zhang, Q. Wu, B. Zheng, J. You and Y. Luo, *Ceram. Int.*, 2018, **44**, 20700–20707.
38 W. Ge, X. Zhang, X. Ge and K. Liu, *Mater. Res. Bull.*, 2021, **141**, 111379.
39 F. Liu, P. Li, J. Li, J. Shi and X. Gao, *Ceram. Int.*, 2024, **50**, 23721–23732.
40 S. D. Zhang, M. J. Yange, K. Y. Liang, A. Turak, B. X. Zhang, D. Meng, C. X. Wang, F. D. Qu, W. L. Cheng and M. H. Yang, *Sens. Actuators, B*, 2019, **290**, 59–67.
41 Z. Zhao, Z. Lv, Z. Chen, B. Zhou and Z. Shao, *Sensors*, 2024, **24**, 2604.
42 J. Ding, Z. Luo, Y. Sun, B. Ren, S. Fu, Y. Yang, J. Cui, X. Wang and J. Yue, *J. Alloys Compd.*, 2024, **1003**, 175736.
43 S. Wang, Q. Liu, J. Shao, G. Pan, Y. Qi and M. Qiu, *J. Alloys Compd.*, 2025, **1010**, 177358.
44 S. M. H. Bagherzadeh Enferadi and A. Mirzaei, *Ceram. Int.*, 2024, **50**, 52861–52870.
45 J. Lee, H. Kim, M. Hilal and Z. Cai, *Solid State Sci.*, 2024, **156**, 107683.